The use of sun elevation angle for stereogrammetric boreal forest height in open canopies

Paul M. Montesano[a,b], Christopher Neigh[b], Guoqing Sun[c], Laura Duncanson[b,c], Jamon Van Den Hoek[d], K. Jon Ranson[b]

Affiliations

a Science Systems and Applications, Inc., 10210 Greenbelt Road, Lanham, MD 20706, USA

b Code 618, Biospheric Sciences Laboratory, NASA Goddard Space Flight Center, Greenbelt MD 20771

c Department of Geographical Sciences, University of Maryland, College Park, MD 20742

d Geography and Geospatial Science, College of Earth, Ocean, and Atmospheric Sciences, Oregon State University, Corvallis, OR, 97331, USA

Keywords: WorldView; sun elevation angle; forest structure; biome boundary; ecotone; taiga; tundra; stereogrammetry; photogrammetry; digital surface model

Abstract

Stereogrammetry applied to globally available high resolution spaceborne imagery (HRSI; < 5 m spatial resolution) yields fine-scaled digital surface models (DSMs) of elevation. These DSMs may represent elevations that range from the ground to the vegetation canopy surface, are produced from stereoscopic image pairs (stereopairs) that have a variety of acquisition characteristics, and have been coupled with lidar data of forest structure and ground surface elevation to examine forest height. This work explores surface elevations from HRSI DSMs derived from two types of acquisitions in open canopy forests. We (1) apply an automated mass-production stereogrammetry workflow to along-track HRSI stereopairs, (2) identify multiple spatially coincident DSMs whose stereopairs were acquired under different solar

geometry, (3) vertically co-register these DSMs using coincident spaceborne lidar footprints (from ICESat-GLAS) as reference, and (4) examine differences in surface elevations between the reference lidar and the co-registered HRSI DSMs associated with two general types of acquisitions (DSM types) from different sun elevation angles. We find that these DSM types, distinguished by sun elevation angle at the time of stereopair acquisition, are associated with different surface elevations estimated from automated stereogrammetry in open canopy forests. For DSM values with corresponding reference ground surface elevation from spaceborne lidar footprints in open canopy northern Siberian *Larix* forests with slopes < 10°, our results show that HRSI DSMs acquired with sun elevation angles > 35° and < 25° (during snow-free conditions) produced characteristic and consistently distinct distributions of elevation differences from reference lidar. The former include DSMs of near-ground surfaces with root mean square errors < 0.68 m relative to lidar. The latter, particularly those with angles < 10°, show distributions with larger differences from lidar that are associated with open canopy forests whose vegetation surface elevations are captured. Terrain aspect did not have a strong effect on the distribution of vegetation surfaces. Using the two DSM types together, the distribution of DSM-differenced heights in forests (μ = 6.0 m, σ = 1.4 m) was consistent with the distribution of plot-level mean tree heights (μ = 6.5 m, σ = 1.2 m). We conclude that the variation in sun elevation angle at time of stereopair acquisition can create illumination conditions conducive for capturing elevations of surfaces either near the ground or associated with vegetation canopy. Knowledge of HRSI acquisition solar geometry and snow cover can be used to understand and combine stereogrammetric surface elevation estimates to co-register and difference overlapping DSMs, providing a means to map forest height at fine scales, resolving the vertical structure of groups of trees from spaceborne platforms in open canopy forests.

1. Introduction

1.1. High resolution spaceborne imagery for forest structure patterns

High resolution spaceborne imagery (HRSI) is the orbital, Earth observation component of the broader class of very-high resolution (VHR) imagery, which includes airborne data. Currently, HRSI

includes primarily multispectral sensors (e.g., SPOT-6 & -7, KOMPSAT-3 & -3A, WorldView-1, -2, -3, & -4) from both the commercial and government sectors. These data can be used to complement forest inventories with detailed characterization of forests across broad extents (Wulder, Hall, & Coops, 2004). Access to commercial HRSI (< 5 m spatial resolution) data (at no direct cost) has been a catalyst for continuing to develop methods for quantifying forest attributes and ecosystem properties (Neigh, Masek, & Nickeson, 2013a). Previous work with optical imagery has highlighted the value of image texture, seasonal brightness differences among image features, and object-based analysis for understanding the spatial patterns of forest structure at multiple scales (Berner et al., 2012; Chopping, 2011; Coburn & Roberts, 2004; Kayitakire, Hamel, & Defourny, 2006; Lamonaca, Corona, & Barbati, 2008; Mallinis, Koutsias, Tsakiri-Strati, & Karteris, 2008; Manninen, Korhonen, Voipio, Lahtinen, & Stenberg, 2009; Ozdemir & Karnieli, 2011; Wolter, Townsend, & Sturtevant, 2009).

1.2. HRSI stereogrammetric estimates of forest canopy surfaces

One use of HRSI is the application of stereogrammetry to estimate surface elevations. Recently, work with this HRSI application has involved detailed surface elevation mapping, characterizing canopy surface elevations, and quantifying height and biomass density in a variety of forests (Baltsavias, Gruen, Eisenbeiss, Zhang, & Waser, 2008; Lagomasino, Fatoyinbo, Lee, & Simard, 2015; Montesano, Sun, Dubayah, & Ranson, 2014; Neigh et al., 2016; 2014; Persson, Wallerman, & Olsson, 2013; Poon, Fraser, & Zhang, 2007; Shean et al., 2016; Vega & St-Onge, 2008). The pointing capabilities of HRSI platforms (e.g., QuickBird, IKONOS, GeoEye-1, WorldView-1, -2, -3, & -4) provide along-track (i.e. near simultaneous) stereoscopic image pairs (stereopairs), where two image acquisitions are captured of the same location from different angles within the same orbit. Stereogrammetry applied to these acquisitions produces fine-scaled (~ 1 m) estimates of the elevation of surface features with pre-registration vertical accuracies of < 4.5 m (Aguilar, del Mar Saldana, & Aguilar, 2014; DigitalGlobe, 2014; Dolloff & Settergren, 2010; Hobi & Ginzler, 2012). Often, HRSI-derived estimates of vertical forest structure are made by linking the canopy surface elevations captured in the stereogrammetrically-derived digital

surface model of elevations (DSM) with coincident estimates of the ground surface elevation from another data source. In remote forested regions, coincident estimates of ground surface elevation beneath the forest canopy are often unavailable or spatially limited. In the open canopy forests along the boreal (taiga) - tundra ecotone (TTE) this results in forest height uncertainties too broad for capturing the vertical component of TTE form and preventing a clear depiction of the differences in the important spatial patterns of structure (Montesano, Sun, Dubayah, & Ranson, 2016). However, in these open canopy forests, there may be an opportunity to exploit the visible ground surface between gaps in tree cover to capture near-coincident ground and canopy surfaces, and thus three-dimensional forest structure, with HRSI. Stereogrammetric forest height estimation is based on this concept of capturing both ground and canopy surfaces from stereogrammetry and examining their differences to explore three-dimensional forest structure.

1.3. HRSI acquisition characteristics

A central feature of HRSI data is the variation in image acquisition characteristics. These characteristics explain the position and orientation of both the imaging platform and the sun relative to the surface targets in the field of view. This sun-sensor-target (SST) geometry describes the average relative position of these components in space at the time of image acquisition. For each image, these include the average off nadir viewing and elevation angles, and the average elevation and azimuth angles of the sun, and surface feature topography. This geometry is influenced in part by the target's diurnal and seasonal sunlight regime, which is a function of the earth's orientation relative to the sun, the target's latitude and topographic position, and the sensor's orientation relative to the sun and the target. As this geometry changes, so does image radiometry both from one image to the next, but also within a given image (Aguilar, Saldaña, & Aguilar, 2013; Epiphanio & Huete, 1995; Honkavaara et al., 2009; Kimes, 1983; Korpela, Heikkinen, Honkavaara, Rohrbach, & Tokola, 2011; Ranson, Daughtry, & Biehl, 1985; Wang, Sousa, Gong, & Biging, 2004; Widlowski, Pinty, & Gobron, 2001).

Due to the off-nadir pointing capabilities of HRSI sensors, SST geometry over the same location can vary widely. This wide variation can affect image radiometry through differences in how features are viewed and illuminated, and thus the appearance of vegetation structure between images (Asner & Warner, 2003; Kane et al., 2008; Wulder, Ortlepp, & White, 2008). This is particularly apparent in summer acquisitions at high latitudes, where the position of the sun throughout the diurnal cycle affects image texture in open canopy forests. In these forests, both forest structure and ground are visible to the sensor. However, the sun's orientation relative to forest structural components (crowns and stems) can be different from that relative to the ground. These changes in orientation not only affect how shadows are cast, but also alter the illumination of surface features such that the difference in brightness (the contrast) between 2 features in one acquisition will not necessarily be maintained in a second acquisition with different SST geometry. These differences can affect the ability to distinguish and measure surface features, such as trees.

In addition to the SST geometry of a single acquisition, stereopairs can be described by additional geometry that explains the orientation of each viewing position with the target. The angles that describe this orientation are the convergence angle, the bisector elevation angle, and the asymmetry angle. The convergence angle, related to the base-to-height ratio (the distance between sensors relative to the height above the target surface), is formed between two observation rays along a plane with the target (the epipolar plane). The bisector angle explains the degree of obliqueness of the epipolar plane relative to the ground plane. The asymmetry angle is the angle formed between the line perpendicular to, and the line that is the bisector of, the line within the epipolar plane that is parallel to the ground plane (Jeong & Kim, 2014; 2016). All three angles affect the horizontal and vertical accuracies of a three-dimensional model. Often, the convergence angle is used to provide a general understanding of the quality of the stereopair geometry for estimating feature heights (Aguilar et al., 2013). The reader is referred to Jeong & Kim 2016 for a detailed description of stereopair geometry and their influence on positioning errors.

The variation in image acquisition characteristics is a feature of HRSI stereogrammetry that provides both an opportunity and a challenge for estimating surface elevations in a variety of land covers.

Given the high spatial resolution (< 1 m) of surface elevation estimates, there is potential for capturing detailed vertical structure in open canopy forests. The challenge lies in identifying the conditions under which features contrast sufficiently with the image background, and understanding both the source of this variation in contrast and the resulting variation in surface elevation measurements.

1.4. Spatial detail in open canopy biome boundary forests

The structure of biome boundary (ecotone) vegetation at the northern limits of the open canopy circumpolar TTE is predicted to change, with important expressions of change controlled by local factors (Bonan, Chapin, & Thompson, 1995; Bonan, Pollard, & Thompson, 1992; Holtmeier & Broll, 2005; Soja et al., 2007). Recent work demonstrates the local scale variability of forest structural change (e.g., height, density and cover) which may be linked to the local spatial pattern of current horizontal and vertical structure of trees (ecotone form) (Harsch & Bader, 2011). At these local scales the effects of topography, wind, disturbance, soil and permafrost characteristics along with long and short term site history (glaciation, fossil treelines, seed availability, soil development, and disturbance) on forest structure patterns are evident, and their relative importance may modify how structure varies across sites (Bunn, Hughes, & Salzer, 2011; Case & Duncan, 2014; Dalen & Hofgaard, 2005; Frost, Epstein, & Walker, 2014; Hofgaard & Wilmann, 2002; Kirdyanov, Prokushkin, & Tabakova, 2013; Lloyd, Bunn, & Berner, 2011). These current forest structure patterns, captured in fine spatial detail with HRSI, may explain the dynamics of structural change across the open canopy biome boundary forests of the TTE (Danby & Hik, 2007; Harper et al., 2011; Harsch, Hulme, McGlone, & Duncan, 2009; Hofgaard, Harper, & Golubeva, 2012; Holtmeier, 2009). Thus, the spatial variability in forest structure patterns, the relevance of these patterns to dynamics and the measurement scales needed to capture these patterns across global domains may warrant remote sensing methodologies with HRSI that are tuned to capture vegetation patterns at scales that drive processes. In the TTE, current site-scale patterns of forest structure across the circumpolar domain may be a precursor to predicting the spatial likelihood of TTE forest structure change, or, TTE structure vulnerability (Epstein et al., 2004).

The measurement of these important structural patterns are challenging in open canopy forests with contiguous, wide area mapping (Duncanson, Dubayah, Cook, Rosette, & Parker, 2015). Lidar measurements alone can resolve tree-level forest structure, but involve trade-offs between spatial detail and measurement accuracy from limitations imposed by the logistics of airborne and spaceborne data collection schemes. For example, while airborne lidar can provide accurate height and canopy detail, and can be used to scale field observations to those of spaceborne sensors, the spatial coverage of such datasets is limited. Furthermore, these data are currently unavailable for vast expanses of Eurasia's permafrost *Larix* forests. Such constraints result in lidar collections that generally address one of two conflicting needs: high-point-density lidar swaths for collecting fine-scale structure across contiguous regional extents, or large footprint lidar for sampling along transects that extend across biomes and continents. Two near-term spaceborne sampling lidar sensors will either not collect data above 52°N (GEDI, The Global Ecosystems Dynamics Investigation) (Dubayah, Goetz, & Blair, 2014; Stysley et al., 2015) or likely characterize open canopy forest structure with high uncertainty (ICESat-2) (Montesano et al., 2015; Neuenschwander & Magruder, 2016). Thus, the mapping of TTE forest structure patterns across a global-scale biome boundary presents a challenge that will not be met with lidar data alone in the current or near-term.

To address this challenge, recent forest structure remote sensing studies have complemented data from spaceborne lidar footprints with imagery. These techniques either spatially group or extend lidar footprint estimates of forest structure (Neigh, Nelson, Ranson, Margolis, et al., 2013b; Nelson et al., 2009; Wulder et al., 2012; Ørka, Wulder, Gobakken, & Næsset, 2012), or link them with image-derived canopy surface elevations (Montesano et al., 2014; 2016; Neigh et al., 2014; 2016; Qi & Dubayah, 2016). Generally, the level of forest structure uncertainty from these techniques is such that they either do not sufficiently resolve site-scale vertical forest structure, or do so only on a per-footprint basis. While uncertainty in structure per se may be a feature of ecological transition zones (Arnot & Fisher, 2007; Hufkens, Scheunders, & Ceulemans, 2009), the subtle structural differences within these zones that describe critical patterns may be required on a continuous (image-level) basis at meter-level spatial scales.

1.5. Objectives

We examined the HRSI DSM estimates of surface elevations in open canopy high-latitude biome boundary forest in the TTE to understand the surface elevation estimates captured in HRSI DSMs from varying stereopair acquisitions. To do this, we applied automated stereogrammetry routines running on a computing cluster to process sub-meter, along-track stereopair imagery across open canopy forests in northern Siberia. We identified multiple sites for which overlapping DSMs were produced. At these sites, we examined (1) the difference in coincident surface elevation measurements derived from imagery acquired under different sun elevation angles in open canopy *Larix* forests, and (2) the potential to exploit sun elevation angle of HRSI acquisitions for capturing continuous (image-based) vertical structure (height) in open canopy forests at scales that reveal important vegetation structure patterns.

2. Methods

2.1. Study area and reference measurements of tree height

We examined the surface elevation estimates from HRSI stereopair collections with different acquisition characteristics for 5 study sites of open canopy forest in northern Siberia (Fig. 1). The study sites are located along the Kotuykan and Kotuy Rivers in the Putorana Plateau and along the Kheta-Khatanga Plain. These sites include open canopy (discontinuous) forests of exclusively *Larix gmelinii* across an elevation gradient from 0 - 350 m.a.s.l., are near the climatic limit of forest vegetation, and coincide with continuous permafrost and the July 10°C isotherm (Osawa & Kajimoto, 2009). *Larix* trees are found within a vegetation matrix that includes tall shrubs (e.g., *Alnus sp., Betula sp., and Salix sp.*) and dwarf shrubs (e.g., *Vaccinium sp.*) and ground cover that includes sedge-grass, moss, and lichen, constituting a range of albedos. Tree cover is generally sparse and ground cover is typically visible in HRSI within the discontinuous forests.

Forest structure measurements were collected in plots along the Kotuykan and Kotuy Rivers in August 2008 (see Montesano et al. 2014, 2016). Plot measurements were coincident with lidar footprints from the Ice, Cloud, and Land Elevation Satellite Global Land Altimeter System (ICESat-GLAS). The

plots used as reference in this study (n = 108) were circular, 10 m - 15 m radius, and geo-located with a horizontal accuracy of +/- 3 m to the centroid of the coincident ICESat-GLAS footprint. In each plot, individual tree measurements included diameter at breast height (DBH, 1.3 m) for each tree > 3 cm DBH, and height. Heights were determined with either a clinometer, a laser rangefinder, or empirically with a linear model relating DBH to height. For each plot, plot-level mean tree height was calculated from its set of individual tree height measurements.

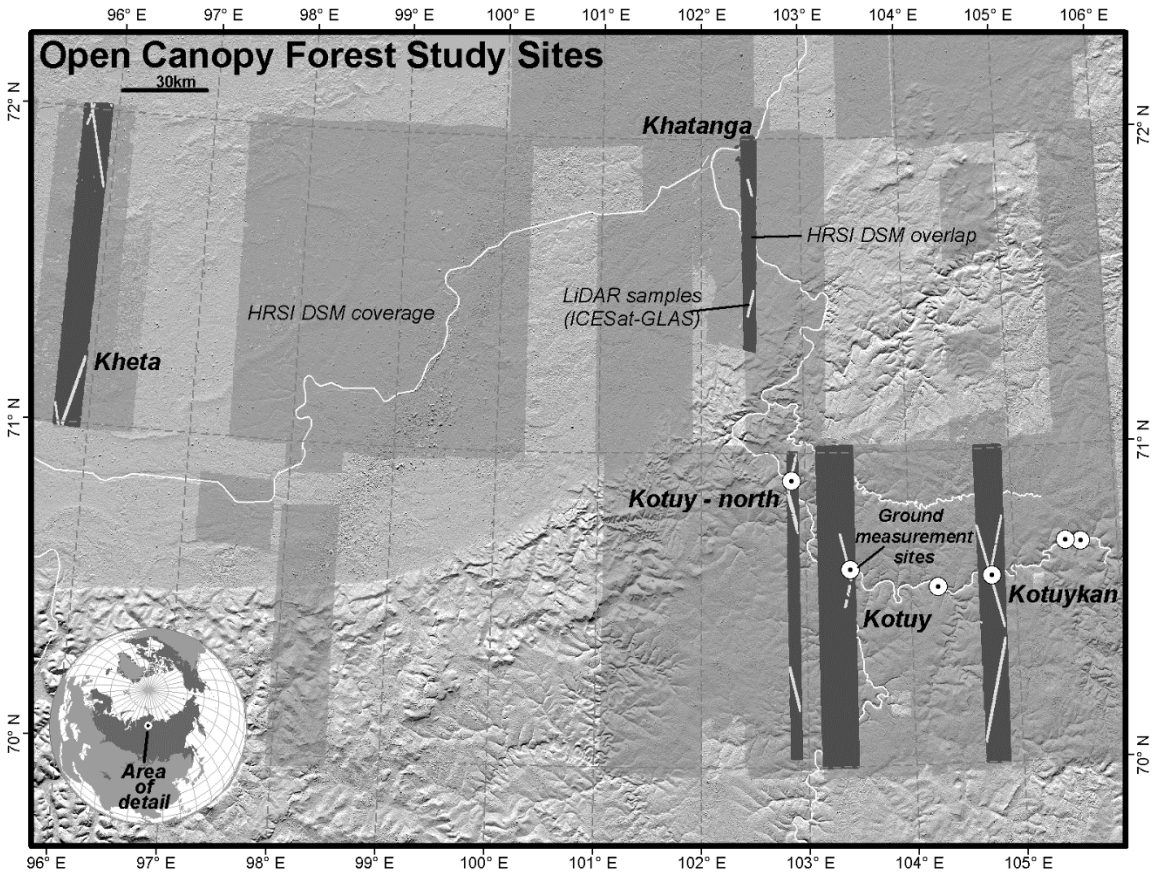

Figure 1. The study sites in open canopy forests in northern Siberia. The light grey regions indicate extents of HRSI DSM coverage, and the 5 dark grey regions indicate the sites (Kheta, Khatanga, Kotuy-north, Kotuy, and Kotuykan) for which overlap of multiple HRSI DSMs provided areas for further surface elevation analysis with ICESat-GLAS lidar footprint transects (white lines) and locations of reference field plots (white circles).

2.2. Regional-scale HRSI data processing

DigitalGlobe provides HRSI at no-direct cost to U.S. Government agencies and non-profit organizations that support U.S. interests via the NextView license agreement (Neigh, Masek, & Nickeson, 2013a). These data are typically available as Level 1B products in compressed National Imagery Transit (NTF) format that, because of data volume, can be cumbersome to examine in large numbers (see Shean et al. 2016 for details) on a standard workstation computer. We used the geographic coverage and associated metadata of DigitalGlobe's Worldview-1, and -2 satellites to identify 1° HRSI strips (each ~ 17 km x 110 km) that formed along-track stereopairs between 70° N - 73° N and 97° E - 106° E. The strip selection was independent of seasonality, but did focus primarily on including nearly cloud-free data (< 20 % cloud cover). These data coincided with areas of open canopy *Larix* forests in and near the TTE.

We deployed automated stereogrammetric routines from the NASA Ames Stereo Pipeline (ASP) v. 2.5.1 (Moratto, Broxton, Beyer, Lundy, & Husmann, 2010; Shean et al., 2016) to mass-produce these HRSI stereopair strips in the NASA Center for Climate Simulation's Advanced Data Analytics Platform (ADAPT, https://www.nccs.nasa.gov/services/adapt). In the ADAPT computing environment, ASP routines were applied to HRSI stereopair strips according to a workflow similar to that outlined by Shean et al. (2016). The pre-processing and stereogrammetry routines in this workflow were applied to the panchromatic stereopairs. This workflow's preprocessing started with the Level 1B correction of WorldView-1 and -2 images of each stereopair to remove sub-pixel offsets that can result in systematic DEM artifacts. Next, these corrected L1B images with the same catalog ID were mosaicked into image strips with updated sensor model information stored in corresponding .XML files. The stereogrammetry portion of the processing involved 4 stages. The correlation stage first pre-aligned the input images with automatic tie-point detection using ASP's affine epipolar method, then computed the correspondences between the pixel of both input images using a kernel of 21 x 21 pixels (a window ~ 10.4 m - 14.7 m on either side) to match features using ASP's normalized cross correlation algorithm. The sub-pixel refinement stage applied ASP's affine adaptive Bayes expectation-maximization algorithm with a kernel of 21 x 21 pixels, which helped resolve the elevation signals from tree crowns. Filtering helped remove

low-confidence values from the previous stage and triangulation produced a three-dimensional point cloud. This point cloud was converted to a DSM at the resolution of the input images, and this DSM was used to orthorectify the more nadir of the two (the "left" image) input stereopair strips. This processing yielded 63 strips of sub-meter HRSI DSM coverage with corresponding orthorectified panchromatic image strips in the regional extent indicated in Figure 1. This set of processed data was used to examine areas of overlap from pairs of two types of DSMs described below.

2.3. Study sites with two types of DSMs

Study areas in open canopy *Larix* forests within northern Siberia were sites for which two types of HRSI DSMs were processed. Each site featured overlap of two types of HRSI DSMs that were described two criteria; the acquisition's sun elevation angle (the angle of the sun above the horizon) and snow cover. The first DSM type included those DSMs whose stereopairs had been acquired with a low sun elevation angle (< 25°; DSM_{sun_low}) and a snow-free ground surface and the second included those acquired with a high sun elevation angle (> 35°; DSM_{sun_high}), regardless of snow cover. These criteria excluded those DSMs with low sun elevation angles and snow-covered surfaces from further consideration, removing the Kotuy-north site from the analysis. At each site, DSMs were paired so that each pair consisted of one DSM of each type. At two sites (Kotuy and Kotuykan), a second DSM was available for one of the DSM types, allowing for a second pair. For example, the Kotuykan site had three available DSMs, the DSM_{sun_low} from 6/4/2013 was paired with the DSM_{sun_high} from 6/4/2013 and also with the DSM_{sun_high} from 6/16/2012, resulting in two pairs for that site. The HRSI DSMs were processed with spatial resolutions ranging from 0.5 m - 0.7 m, referenced to the WGS84 ellipsoid, and projected to the local zone (48N) of the Universal Transverse Mercator projection.

2.4. Vertical co-registration of DSM values with lidar surface elevation estimates

The DSMs each have a unique vertical bias (DigitalGlobe 2014). As such, coincident DSMs are offset from one another and require co-registration to vertically align them before their spatially coincident elevation values can be compared. We used coincident ground surface elevation estimates

from lidar footprints (nominally 60 m in diameter, spaced 172 m along-track, with a horizontal geolocation accuracy < 4.5 m) from the ICESat-GLAS global land surface altimetry product (GLA14) as control to vertically co-register overlapping DSMs (Zwally et al., 2002; 2014; Duong et al., 2009). The surface elevation estimate for each lidar footprint is derived from the footprint's waveform, which is a representation of the vertical distribution of laser energy returned to the sensor with a 15 cm resolution. The GLA14 product describes this waveform with signal begin and end elevations, and 6 gaussian peaks. The waveform has a length calculated as the distance between the signal beginning and end above a noise threshold that indicates the vertical range across which elevations were recorded within the footprint (Sun et al. 2008). The waveform's first gaussian peak generally provides an estimate of the ground surface elevation. In these sparse forests, this first peak dominates the signal such that the waveform's centroid provides an estimate of near-ground surface elevation, which is assumed to closely represent the DSM's surface elevation estimate. This waveform-derived surface elevation estimate for each lidar footprint provided reference elevations for the DSM co-registration, which was a multi-step spatial and statistical procedure. This procedure involved for each site (1) identifying lidar footprints coincident with the area of intersection between the site's DSMs to provide a basis for co-registration, then (2) calculating a DSM-specific co-registration factor to account for the vertical bias of each DSM using lidar footprints, and (3) applying the co-registration factor to original DSM values.

First, we spatially linked DSM elevations to lidar footprints, as follows. For each pair of DSMs, the intersection area common to all DSMs of the pair was identified. Within this area, the surface elevation from each lidar footprint (L_i) was collected from the centroid of each footprint's waveform and registered to the WGS84 ellipsoid ($L_{i,\ cntrd}$), the same vertical datum referenced by each DSM. Lidar footprints with a waveform length > 20 m were removed from the dataset to exclude footprints contaminated with clouds or aerosols. For each remaining footprint, a 25 m x 25 m window centered on the footprint's centroid was used to represent each footprint's spatial extent within which we calculated the mean DSM surface elevation, mean DSM slope, and mean DSM aspect. Each footprint's slope and aspect values were derived from each DSM that was coarsened to a pixel size 5% of the input resolution,

resulting in a coarsened DSM spatial resolution of 10 m - 14 m to remove the fine-scale slopes associated with elevation changes from individual tree canopies and other small features on the landscape. Since each lidar footprint overlapped multiple coincident DSMs, the slope and aspect values assigned to each footprint were derived from the DSM_{sun_high} of a given DSM pair, and were grouped according to two categories of slopes ($<$ 10° and $\geq$ 10°) and four categories of aspect (>315° & ≤ 45°, *north*; >135° & ≤ 225°, *south*; > 45° & ≤ 135°, *east*; > 225° & ≤ 315°, *west*). Footprints on slopes ≥ 10° (~ 3% of footprints) were excluded from further analysis. These lidar-footprint-level calculations were added to a database that included the geographic coordinates of each lidar centroid, the $L_{i,\ cntrd}$ value, and the mean DSM elevation, slope, and aspect. This database was linked to a DSM-level database that included information on stereopair acquisition.

Second, a gaussian-peak approach was used to co-register elevations from overlapping DSMs. We used lidar as vertical control in an algorithm that estimates a DSM-specific co-registration factor to align DSM ground surfaces, creating a basis for the surface elevation comparisons between overlapping DSMs. For each lidar footprint (L_i), we calculated the difference ($L_{i,\ dif\_lidar}$) of each footprint's mean DSM value within the 25 m x 25 m window ($L_{i,\overline{DSM}}$) from $L_{i,\ cntrd}$ for each DSM coincident with the lidar footprint. The many footprints associated with each DSM provided a distribution of $L_{i,\ dif\_lidar}$ values. Then, for each DSM, we analyzed the distribution of these $L_{i,\ dif\_lidar}$ values. We compiled a histogram of each DSM's $L_{i,\ dif\_lidar}$ values and fit three gaussian curves using the '*normalmixEM*' function in the '*mixtools*' package in R (Benaglia, Chauveau, & Hunter, 2009; R Core Team 2013). This curve-fitting procedure helped to identify sub-groups within each $L_{i,\ dif\_lidar}$ distribution that were statistically distinct. Each sub-group has a mean difference from $L_{i,\ cntrd}$ and was assumed to represent a unique group of surfaces (e.g., near-ground, vegetation) captured by lidar footprint sampling of the DSM values returned from the stereogrammetry analysis.

We used the mean of the first gaussian peak ($\mu_{DSM,pk1}$) to identify the sub-group within each $L_{i,\ dif\_lidar}$ distribution that had the smallest mean difference from $L_{i,\ cntrd}$, and used this peak's standard

deviation ($\sigma_{DSM,pk1}$) in the following equation for a DSM-specific co-registration factor (CF_{DSM}). The co-registration factor shown in Equation 1 helps account for the effect that vegetation canopy surfaces may have on the difference between DSM surface elevations and ground surface control. A value of 3.5 is used to indicate the far left portion of the distribution that exploratory work suggested was closely associated with the ground surface:

$$CF_{DSM} = \mu_{DSM,pk1} - \lfloor 3.5 \times \sigma_{DSM,pk1} \rfloor \qquad \textit{Equation 1}$$

Third, each CF_{DSM} was applied to systematically shift original mean DSM values summarized in each lidar footprint. This vertical co-registration of each lidar footprint's DSM value with a reference near-ground surface provided by $L_{i,\,cntrd}$ was calculated with Equation 2:

$$L_{i,DSM_{cor}} = L_{i,\overline{DSM}} - CF_{DSM} \qquad \textit{Equation 2}$$

2.5. Comparison of co-registered DSM values with lidar

After vertical co-registration, we compared $L_{i,DSM_{cor}}$ values of each DSM type across the study sites. Each site's set of corresponding lidar footprints provided the locations used to compile distributions of the difference of the co-registered DSM values from reference ground surface elevation as shown in Equation 3:

$$L_{i,\,ht_{spc}} = L_{i,\,DSM_{cor}} - L_{i,\,cntrd} \qquad \textit{Equation 3}$$

The $L_{i,\,ht_{spc}}$ value is a combined DSM and lidar height measurement. It represents the difference between a DSM measurement from that of the lidar ground surface and can be used to examine the heights of features above the ground that the DSM has captured.

2.6. Differencing co-registered DSM values

Equation 4 shows the DSM-differenced height measurement $L_{i,\,ht_{DSMdiff}}$ calculated for each lidar footprint. This calculation is arranged according to DSM type, where the sun elevation angle of the HRSI stereopair acquisition used to compile each DSM dictates how DSM values are differenced. The

collection of footprints for which $L_{i,ht_{DSMdiff}}$ was computed was used to examine the distribution of DSM-differenced heights.

$$L_{i,ht_{DSMdiff}} = L_{i,DSM_{sun\_low}} - L_{i,DSM_{sun\_high}} \quad \textit{Equation 4}$$

The distribution of these DSM-differenced heights was shifted as in Equation 2, using the gaussian-peak approach described in Equation 1. Here, the mean and standard deviation values are derived from the first gaussian peak of the DSM-differenced heights from each pair of DSMs. Each shift is specific to each DSM pair, and was applied to the image-level DSM differencing to map forest heights.

2.7. Classification of lidar footprints

To further understand the surface elevations captured from each DSM type we identified lidar footprints associated with open canopy forest or otherwise. To do this, we classified a portion (33%) of the footprints across the study sites into '*forest*' or '*non-forest*' cover types using the 0.5 m - 0.7 m resolution panchromatic orthorectified imagery associated with each site. The footprints classified as '*forest*' were those determined as being at least partially corresponding to tree cover, while those footprints classified as '*non-forest*' likely featured a mix of ground covers such as lichen, sedge, or low shrubs. This classification allowed for an examination of which lidar footprints likely featured surface elevations influenced by open canopy forest as well as how surface elevations from each DSM type compared within these general cover classes.

3. Results

3.1. Overview

For our study sites, we summarize the DSM acquisition characteristics. For sites with valid DSM type pairs, we (1) report surface elevation errors, relative to reference lidar-derived footprint surface elevations, for each DSM based on type and terrain aspect, (2) compare distributions of the difference between DSM elevations and reference lidar for each DSM type across all sites and '*forest'* and '*non-forest'* classes, and (3) corroborate the distribution of DSM-differences (heights) at reference lidar

363 footprints with field-based plot-level mean tree height measurements and provide examples of DSM-
364 difference maps of open canopy forest height within the study sites.

365 **3.2. DSM acquisition characteristics**

366 In the northern Siberia study region, 17 individual HRSI DSMs across 5 sites of overlap were
367 considered in this analysis (Table 1). Of these 5 sites, 4 featured valid DSM type pairs (DSM_{sun_high} and
368 DSM_{sun_low}) for which the DSM_{sun_high} was free of snow cover (the Kotuy-north site did not). At all 5 sites
369 the surface elevation estimates from individual DSMs with reference lidar ground surface elevation
370 estimates for open canopy *Larix* forests helped explain the surfaces with which elevation measurements
371 from the two types of DSMs were associated.

372 Initial results provided examples of how acquisition characteristics of HRSI may influence DSM
373 results from automated stereogrammetry. In Figure 2, the top row shows a representative subset of
374 panchromatic HRSI from two different WV01 stereopairs collected within ~ 1 day at the same location in
375 open canopy *Larix* forests. Here, vegetation and ground conditions are similar given the near
376 simultaneous acquisition of both stereopairs. The bottom row shows the corresponding color-shaded relief
377 image of the DSM. The left (7/11/2012) and right columns were acquired at high (> 35°) and low (< 25°)
378 mean sun elevation angles, respectively. This subset from within the Khatanga site provides an example
379 of the DSM types that were used across all sites in this study.
380
381
382 **Table 1**. Summary of HRSI DSM acquisition characteristics and the associated number of lidar footprints
383 at 5 sites with overlap between DSM_{sun_high} and DSM_{sun_low}. The DSMs at the Kotuy-north site were
384 excluded from the subsequent analysis because the site lacked valid DSM type pairs. Note: HRSI DSM
385 names are comprised of satellite platform, acquisition date, and the catalog IDs of each of the two
386 stereopair images (the first catalog ID is conventionally the more nadir of the two). All DSMs across the
387 study sites had convergence angles between 30° and 60°.

HRSI DSM Name	*Stereopair Acquisition Date*	*Site*	*Condition*	*Mean Sun Elev. Angle (°)*	*Lidar footprints (#)*
WV01_20120602_102001001A7B6F00_102001001C395800	6/2/2012	Kotuy	snow	42	313
WV01_20120616_102001001B6B7800_102001001A4BEC00	6/16/2012	Kotuykan	snow-free	43	2165
WV01_20120710_102001001CE5F900_102001001CE3A400	7/10/2012	Khatanga	snow-free	8	323
WV01_20120711_102001001C88E300_102001001CDB0B00	7/11/2012	Khatanga	snow-free	41	323
WV01_20120808_102001001C790F00_102001001CE43800	8/8/2012	Kotuy-north	snow-free	36	616
WV01_20121007_102001001DA1E400_102001001F138E00	10/7/2012	Khatanga	snow	13	323
WV01_20130216_102001001FC1D000_10200100212F9F00	2/16/2013	Kotuy-north	snow	7	616
WV01_20130226_102001002163B600_102001001F57B800	2/26/2013	Kotuy-north	snow	11	616
WV01_20130604_102001002138EC00_1020010021AA3000	6/4/2013	Kotuykan	snow-free	8	2165
WV01_20130604_1020010023E3DB00_1020010024C5D300	6/4/2013	Kotuykan	snow-free	42	2165
WV01_20130724_10200100246B6B00_1020010022D9CD00	7/24/2013	Kotuy	snow-free	5	313
WV01_20140307_102001002A803800_102001002ADD4300	3/7/2014	Kotuykan	snow	14	2165
WV02_20130309_1030010020632700_103001002065A800	3/9/2013	Kotuy-north	snow	15	616
WV02_20130719_1030010025AD6800_10300100250F1100	7/19/2013	Kheta	snow-free	9	1022
WV02_20130729_103001002575BC00_1030010024955700	7/29/2013	Kheta	snow-free	37	1022
WV02_20130915_1030010026161400_1030010026B60000	9/15/2013	Kotuy	snow-free	23	313
WV02_20131025_1030010027457800_1030010028BBC900	10/25/2013	Kotuy	snow	7	313

388

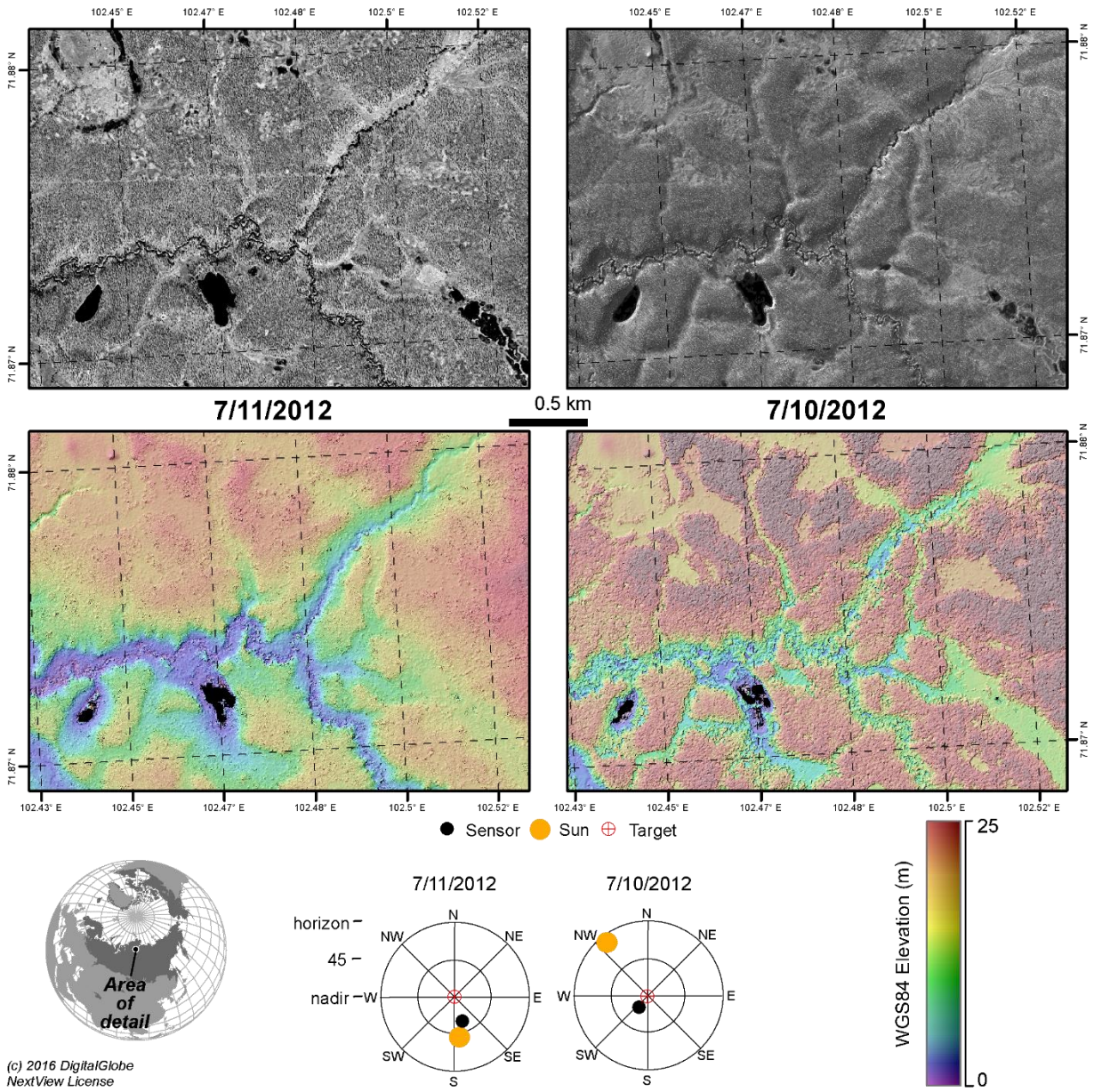

389

390 **Figure 2**. DSMs of the same location from stereopair acquisitions with different sun elevation angles. A
391 subset of the Khatanga study site for which stereopairs were collected on each of two successive days in
392 July 2012. The top row shows the panchromatic image for July 11 and 10th, and the bottom row shows
393 their corresponding color-shaded relief image of the DSM. HRSI acquisition geometry describing the
394 relative position of the sun and the sensor to the image (target) associated with one image of each
395 stereopair is shown in the corresponding polar plots. The corresponding images (not shown) for

7/11/2012 and 7/10/2012 have satellite elevation and azimuth angles of 64°& 80° and 59° & 308°, respectively.

3.3. Surface elevation errors

DSM elevation errors were derived from linear models built from reference surface elevation estimates from 4,439 lidar footprints, for 17 DSMs across the 5 study sites. For all 17 DSMs, Figure 3 summarizes the root mean square error (RMSE) from linear models relating DSM and reference elevations collected at lidar footprints, and distinguishes the 6 DSMs (hollow circles with an 'X') associated with the type DSM_{sun_low} that also featured snow cover (i.e., winter acquisitions, October through March). The magnitude of these RMSEs, by DSM type, are < 0.68 m for DSM_{sun_high}, > 1.0 m for all DSM_{sun_low} and > 1.5 m for those DSMs in DSM_{sun_low} with mean sun elevation angles < 10°. Within the DSM_{sun_low} type the outlier with a RMSE of 1.03 m and a mean sun elevation angle of 23° is a mid-September (9/15/2013) acquisition.

At the 4 sites with valid DSM type pairs, linear models were computed for 4 terrain aspect categories for all lidar footprints (3,823) associated with each of the 10 valid DSMs at these sites. Figure 4 indicates that there is a strong difference between DSM values collected with different sun elevation angles, but little difference across terrain aspect categories. These models were bootstrapped to understand the uncertainty of the distribution of model RMSEs. Bootstrap results suggest that, within each terrain aspect category, there are differences between DSM type in the errors of DSM surface elevation estimates relative to reference lidar ground surface estimates. However, while RMSEs suggest differences between the two DSM types, within each type the terrain aspect category 95% CIs for the model RMSEs generally do not suggest significant differences.

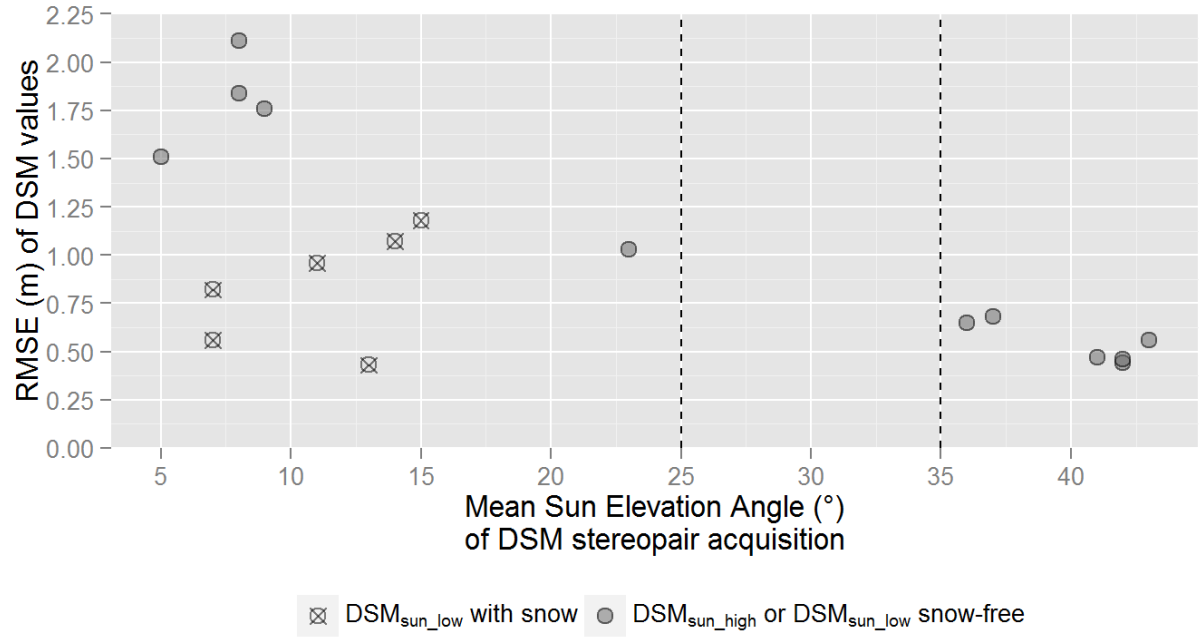

417

418 **Figure 3**. Comparison of DSM elevation errors with reference lidar elevations. The RMSE values were
419 derived on a per-DSM basis (each dot corresponds to one DSM) from linear models built from the
420 relationship of original mean DSM values with reference surface elevations from lidar footprints.
421 Vertical dashed lines indicate the upper and lower bounds of the DSM_{sun_low} and DSM_{sun_high} types,
422 respectively.

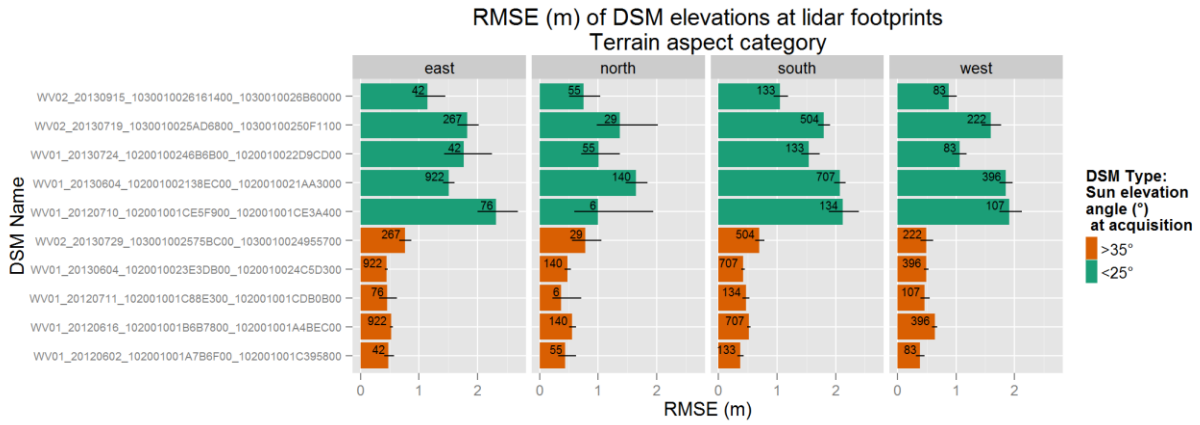

423

424 **Figure 4**. Lidar footprints provided reference ground surface elevation estimates to examine the influence
425 of terrain aspect on DSM errors. The magnitude of the RMSE from the linear model of each DSM's

elevations to those of corresponding lidar ground surface are summarized. The error bars (black lines) indicating the bootstrapped 95% confidence interval of the RMSE and number of lidar footprints on which each DSM's model was built are shown for each DSM. Individual DSMs are grouped according to DSM type.

3.4. Vertically co-registered surface elevations

Vertical co-registration was applied to 10 DSMs across the 4 sites. This co-registration amounted to a DSM-specific shift (translation) in elevation values that vertically aligned coincident locations between DSMs using lidar surface elevations as reference. The distribution of surface elevation differences provide an assessment of the surface heights estimated from each DSM type above the assumed ground reference from lidar. These surface elevations differences between DSM types show important differences.

In Figure 5, distributions of the differences between co-registered DSM elevations and reference lidar ground surface elevations are grouped by site. These groups reveal a consistency in the difference in surface elevation estimates according to DSM type. The histograms show the distribution of corrected DSM values according to DSM type, for each study site where both DSM types were available. At these sites, distributions of differences between values from DSM_{sun_low} (green bars) and lidar show skewed distributions, reflecting a broad range of differences in surface elevations relative to reference lidar. Those distributions of differences between values from DSM_{sun_high} (brown bars) and lidar are more compact. At 2 sites (Khatanga and Kotuykan), Kolmogorov-Smirnov (KS) tests indicated differences between the distributions from each DSM type are significant ($p < 0.05$). At the 2 remaining sites (Kheta and Kotuy), KS tests did not indicate significant differences in the distributions from each DSM type. While these 2 sites feature skewed curves from each DSM_{sun_low}, evidence of vegetation surfaces influencing the difference distribution, they also feature peaks at differences around 1.0 m. These peaks suggest that a large portion of sampling at these sites was done in *non-forest* land cover, where DSMs will feature near-ground surface elevations regardless of sun elevation angle.

Surface elevation difference distributions for lidar footprints classified as *'forest'* support the difference in measurements between the two DSM types. Figure 6 shows a comparison between the distributions of each DSM type from footprints in two general land cover classes. Footprints from *non-forest* portions of the study area indicate similar distributions (KS test $p > 0.99$). Conversely, footprints from open canopy forests show significant differences in these distributions (KS test $p < 0.05$). The difference distribution of the *'forest'* footprints from DSM_{sun_low} (green bars), which represent the forest height estimates at the lidar footprint locations ($\mu = 6.0$ m, $\sigma = 1.4$), is within 1 σ of the distribution of plot-level mean tree heights (gray bars; $\mu = 6.5$ m, $\sigma = 1.2$ m).

Figures 5 and 6 show differences in the distributions of surface elevation differences between DSM types across sites, and within *'forest'* footprints. These differences, along with the similarity of spaceborne forest height estimates with those from reference plot measurements suggests that, in open canopy forests, DSM_{sun_low} are capturing forest surfaces above those of the near-ground surface from the reference lidar while DSM_{sun_high} provide near-ground surface elevations.

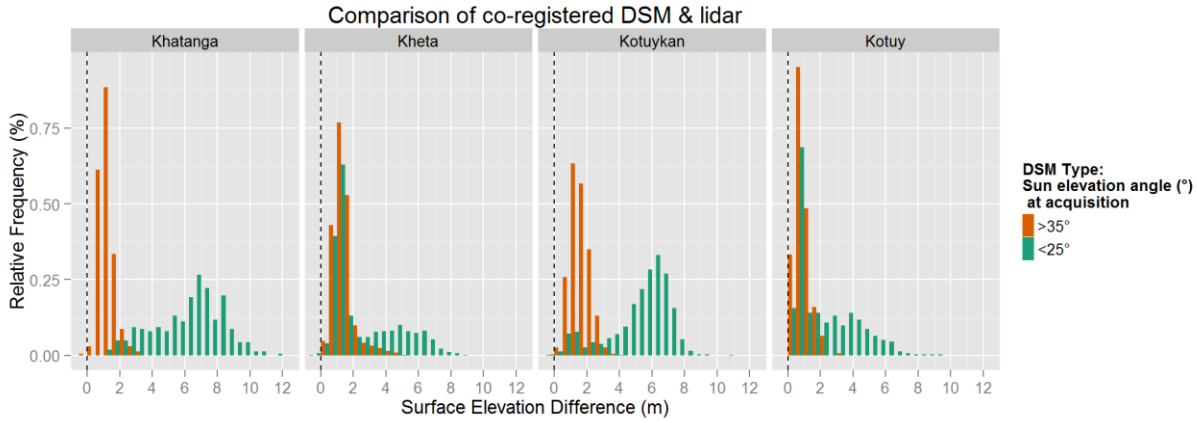

Figure 5. Comparison of co-registered elevations from DSMs and lidar footprints, by study site. These relative frequency distributions, grouped according to DSM type, show the difference of co-registered DSM elevation values from those of reference lidar, for each of the 4 study sites.

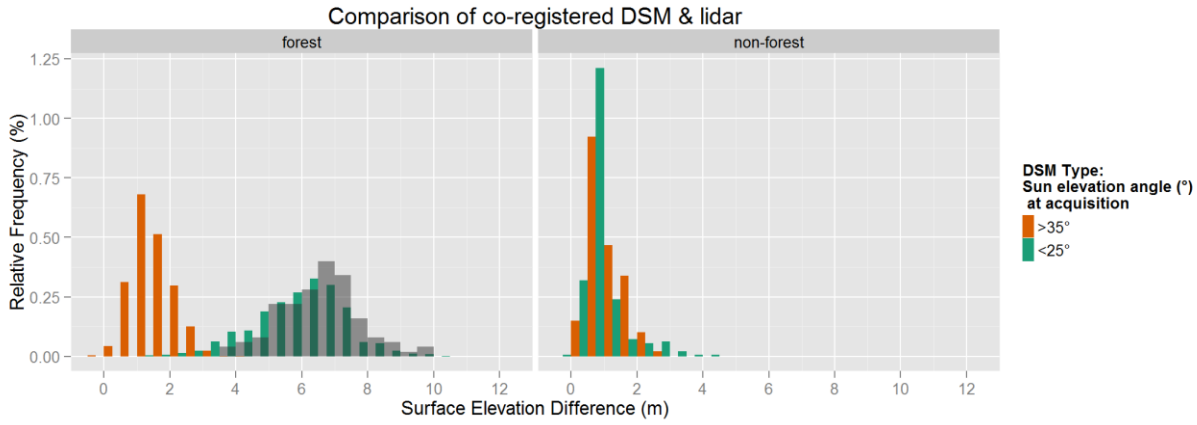

Figure 6. Comparison of co-registered elevations from DSMs and lidar footprints, by land cover class. These relative frequency distributions, grouped according to DSM type, show the difference of co-registered DSM elevation values from those of reference lidar, for the set of footprints that were classified into one of two general land cover classes, '*forest*' or '*non-forest*'. In the '*forest*' plot, the gray bars represent plot-level mean tree heights.

3.5. DSM-differenced heights in open canopy forests

Figure 7, showing the DSM-differenced heights at all lidar footprint locations, shows the range of footprint height estimates across the 4 study sites. The left facet combines the distributions of the classified lidar footprints, '*forest*' and '*non-forest*', shown in Figure 6 with '*unclassified*' footprints. The right facet summarizes the distribution of the reference plot-level mean tree heights ($\mu = 6.5$ m, $\sigma = 1.2$ m). A general uncertainty in these height estimates is highlighted by the peaks towards the bottom of the left facet associated with footprints labelled '*non-forest*' and '*unclassified*'. This general uncertainty reflects the uncertainty in elevation estimates from each DSM, is provided by the RMSE of the DSM_{sun_high}, and represents the error of the surface elevation estimates of the ground. These errors (< 0.68 m, Figure 3) represent primarily footprints of near-ground surfaces yet show height values > 0. This uncertainty estimate is a mean on a per DSM basis, and does not include the uncertainty associated with the forest canopy surface from DSM_{sun_low}.

Figure 8 shows mapped examples of forest height resulting from image-level DSM differencing. At each study site, forest height is mapped across ~ 7 km^2 of open canopy forest, and are comprised of pixel-level estimates at a spatial resolution of 2 m. These representative examples show how forest height varies across scales of tens of meters at these sites, and how these variations in height reveal a different forest structure patterns across the maps.

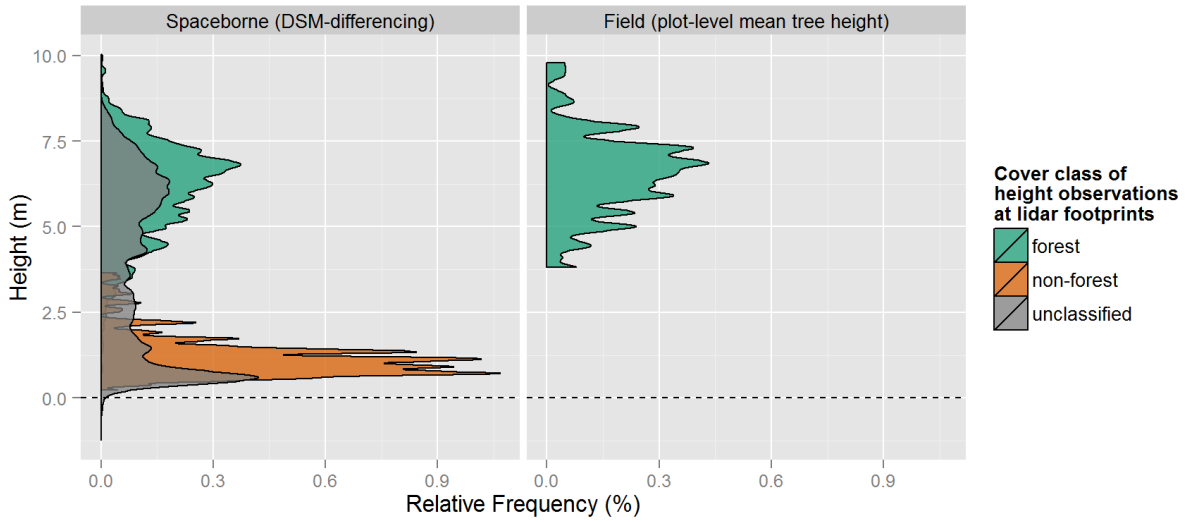

Figure 7. The relative frequency distributions of two types of height observations at lidar footprints. The left facet shows the height distributions from spaceborne DSM-differencing at unclassified, '*forest'* and '*non-forest'* footprints. The right facet shows field-derived plot-level mean tree heights in open canopy forest plots in northern Siberia. The portion of the lidar footprints were classified as '*forest*' and '*non-forest'* to underscore the difference in heights from these two groups, and the spaceborne heights are shown adjacent to those from field measurements to illustrate the similarity in forest heights between the two.

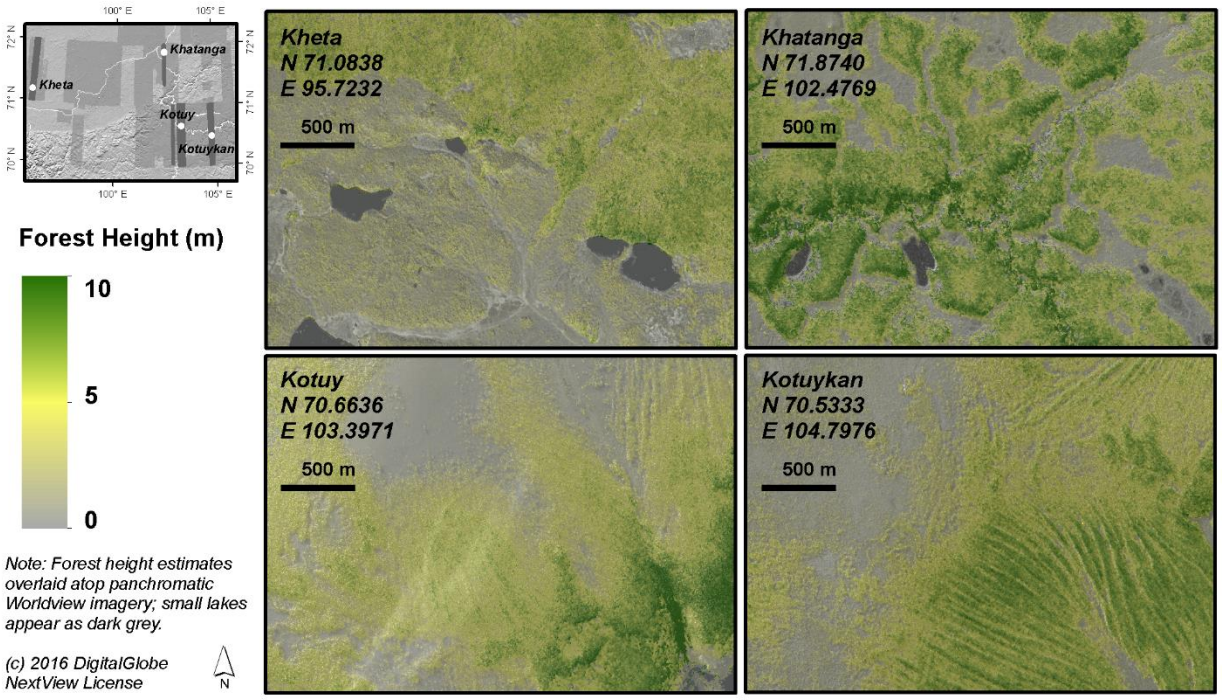

499

500 **Figure 8**. Mapped examples, each ~ 7 km^2, of DSM-differenced heights in open canopy forests in
501 northern Siberia. Forest height estimates are presented at 2 m spatial resolution from image-level DSM
502 differencing applied after vertical co-registration of DSM pairs at each study site. Shown at the spatial
503 scale of large groups of trees, each example shows the pattern of forest structure that is revealed with
504 mapped forest height across sites.

505 ## 4. Discussion

506 ### 4.1. Overview

507 Acquisition sun elevation angle is an important consideration for stereogrammetric estimates of
508 forest structure in open canopies. The combination of HRSI DSMs derived from different solar
509 illumination conditions in open canopies can provide meter-level vertical forest structure
510 information. This structure is captured when a difference in sun elevation angles among overlapping
511 HRSI stereopair acquisitions provides an important source of variation in surface elevation estimates from
512 the resulting DSMs. There are 4 main results from this work. First, within lidar footprints, co-registered
513 HRSI DSM values derived from automated stereogrammetry can produce different surface elevations for

514 a given location within open canopy forests, and terrain aspect categories on slopes < 10° did not result in
515 large differences in errors. Second, in these forests this variability is in part associated with sun elevation
516 angle whereby high angles (> 35°) can result in DSMs that are more closely related to near-ground
517 surface elevations (RMSEs < 0.68 m) and low angles (< 10°) capture characteristics of the vertical
518 structure of open canopy forests. Third, high latitude DSMs acquired in winter, when sun elevation
519 angles are low and snow covers the ground, can provide an important exception to this general rule in
520 open canopy forests. Fourth, when these two types of DSMs spatially and temporally overlap, the
521 difference of their vertically co-registered values is closely related to vertical vegetation structure (in this
522 case, plot-level mean tree heights) in open canopy forests.

523 Surface elevation estimates from individual DSMs did not vary significantly between terrain
524 aspect categories on slopes < 10°. However, within each aspect category the bootstrapped RMSEs of
525 elevation values relative to lidar reference of near-ground surface elevations are consistently larger from
526 individual DSMs collected at low sun elevation angles as compared to those collected at high angles.
527 When broken down by aspect category, these errors support the RMSE results from the level of individual
528 DSMs. These consistently larger errors, relative to lidar reference, from individual DSM_{sun_low} values
529 versus those from DSM_{sun_high}, suggest an influence from aboveground vegetation surfaces on surface
530 elevations computed with automated stereogrammetry. Thus, one feature of the solar geometry at the time
531 of stereopair acquisition (sun elevation angle) may indicate which surfaces, near ground or vegetation, are
532 captured with the elevation estimates from the resulting DSMs in open canopy forests.

533 These vegetation surfaces, particularly tree canopies, influence the image correlation portion of
534 the automated stereogrammetry in ASP, and thus affect elevation measurements under certain
535 circumstances. Automated image correlation looks for similar patterns in image brightness between the
536 left and right images of each stereopair in order to match image pixels corresponding to the same feature.
537 To distinguish a difference in surface elevation of vegetation from the elevation of the ground surface
538 itself, there must be a sufficient difference in image brightness (i.e., contrast) between the feature and the
539 ground to determine parallax (Oleg Alexandrov, personal communication). If the ground and vegetation

have similar spectral properties (i.e. brightness) ASP would likely be unable to identify the top of the feature, and thus the surface elevation measurement at the feature's location would be more representative of the ground (background) elevation. Therefore, the contrast in brightness between vegetation and the ground surface primarily determines whether elevations from stereopairs are derived from somewhere at the top or within the canopy, or from the ground. For stereopairs collected at low sun elevation angles, the sun illuminates the sides of tree canopies more directly than the ground surface, producing the contrast needed to distinguish between ground and vegetation. Conversely, when sun elevation angles are high, the contrast between vegetation canopy surfaces and ground typically decreases. This helps produce a smoother DSM where canopy surfaces have a reduced influence on the elevation measurement, and thus the DSM represents a surface more closely related to the ground.

From these results in open canopy boreal forests, we recommend filtering stereo acquisitions for high sun elevation angles (> 35°) to produce digital terrain models (DTMs) of ground surface elevations, and low sun elevation angles (< 25°) to produce DSMs that include surfaces associated with vegetation height. In fact, we note that most of our low sun elevation DSMs were < 10°, with only a single DSM outside that range (23°). We also note that these recommendations are potentially limited to the range of observations in this study. In areas where the difference in brightness between vegetation and underlying terrain is affected by snow cover, fire, recovery from fire, differences between understory and overstory, or where canopy covers are relatively closed, these recommendations may not hold. Indeed, results from winter imagery (low sun elevation angles) with complete snow cover yielded inconsistent canopy surface elevations across DSMs when compared to similar types of DSMs derived from snow-free imagery.

We note two particular lines of analysis that were not part of this study that could improve our understanding of the utility of HRSI stereopairs and the uncertainties of their estimates of vertical forest structure in open canopies. First, a closer look at the tree canopy cover interval in which the DSM-differencing methodology is applicable should be addressed. This will clarify for which types of open canopies this methodology should be applied, and, importantly, where it will not be able to capture vertical structure. Second, the interaction effects of stereopair SST geometry on height estimates are not

entirely clear. Further analysis into the relationships between the contrast in image feature brightness from ground and vegetation, due to either differing illumination angles or shadowing, should be addressed. Such an inquiry would better capture the influence from the orientation of a local plane as well as the horizontal and vertical uncertainties associated with a variety of sun-sensor-target geometries. Such work will improve the use of HRSI DSMs for describing detailed surface feature elevations.

4.2. The advantages of a variety HRSI acquisitions: forest structure at biome boundaries

A variety of spatially coincident HRSI stereopair acquisitions, at both high and low sun elevation angles, provide opportunities to capture detailed vertical structure patterns in open canopy forests across broad spatial scales. Such open canopy forest cover is a feature at forest biome boundaries, where subtle vegetation patterns can reflect ecologically important differences in surface characteristics that are not otherwise apparent in remotely sensed imagery. While differing illumination conditions of images often interfere with the interpretation of land cover type, vegetation health and change, and create a need for solar illumination and terrain correction, such characteristics are a feature of remote sensing data to be exploited with regard to interpreting vegetation structure. In particular, this feature of HRSI can serve the objective of capturing spatially continuous fine-scale estimates of forest structure patterns across broad scales. Ongoing work includes mining the mounting archives of HRSI stereopairs to identify data with optimal solar illumination geometries for open canopy forest structure, and subsequently to sample and map forest structure characteristics at the scale of spatial change across the biome boundaries. This will help to both quantify and refine forest patterns and improve predictions of ecosystem dynamics.

4.3. The implications for mass-production of surface elevation models

Open canopy boreal forests cover large portions of the Arctic, where HRSI surface elevation modelling is ongoing. Such modelling may be able to exploit certain characteristics of solar geometry to target surface features of interest. Our results, which suggest that ground surface can be more closely represented in open canopy forests from acquisitions that coincide with high sun elevation angles, may help refine the HRSI input for such surface modeling. Refining HRSI input may provide a more accurate

591 terrain reference, because the vertical structure of discontinuous forest canopy may be less likely to
592 interfere with stereogrammetric estimates of ground elevations within the context of automated
593 processing. Refining HRSI input within mass-production workflows is provides a powerful combination
594 of large volume processing that identifies the most scientifically useful datasets that exist within vast
595 archives. There is an opportunity to mine the archive of HRSI stereopairs to identify images with
596 acquisition characteristics that are more likely to improve DSM estimates of surfaces of interest, and then
597 prioritize those datasets. This mining strategy can continue to be updated as more is learned about the
598 sources of uncertainty of HRSI data products, and how they can be minimized.

599 **4.4. Relevance of HRSI stereopairs in the observation of biome boundary forests**

600 HRSI stereopairs from passive optical platforms have the potential to fill an important
601 observation gap in the spaceborne observation of biome boundary forests. Not only do these datasets
602 provide spatial resolutions that permit monitoring of forests at fine scales, but they provide this detailed
603 monitoring across global extents. A prominent biome boundary, the boreal-tundra transition forests of the
604 TTE, has a relative dearth of spaceborne data capable of resolving vertical structure in its relatively sparse
605 and short stature forests (the spaceborne lidar dataset from ICESat-GLAS notwithstanding). One primary
606 limitation to their use is the availability of spatial overlap among the types of acquisitions needed for
607 capturing vertical forest structure patterns.

608 Nevertheless, these HRSI data should be part of a data integration scheme for the remote and
609 subtle vegetation structure signals in high northern latitudes. This is due in part to the likelihood that
610 current and near-term missions may either be unable to reach or resolve these regions. The upcoming
611 Global Ecosystem Dynamics Investigation (GEDI) mission will be mounted on the International Space
612 Station, and thus only acquire data up to ~ 51.5° N. ICESat-2 (to be launched ~ 2018) will collect data
613 over the circumpolar boreal domain, but its ATLAS photon counting sensor will only collect a sparse
614 return of photons. Converting these weak lidar returns to vegetation structure information will be
615 challenging. Its primary value, which should not be understated, may likely be to provide added ground

surface reference to those existing GLAS estimates, an important complement to HRSI DSMs for purposes of characterizing forest structure. High resolution data (from airborne lidar or HRSI) may provide a basis for testing the ability of ICESat-2 to capture the vegetation canopy in these sparse forests, but political restrictions prevent airborne campaigns from accessing most of the Eurasian boreal. Polarimetric synthetic aperture radar interferometry (eg., from Tandem-X) has advantages over lidar in terms of spatial coverage and has shown promise for providing forest height estimates in boreal regions (eg., Chen et al. 2016, Olesk et al. 2016), but these estimates are at spatial resolutions of tens of meters, an order of magnitude larger than those estimates available from current HRSI stereopairs from passive optical platforms. Therefore these HRSI stereopairs become even more important, allowing us to monitor this changing and challenging ecosystem at the spatial resolution necessary to monitor fine scale processes.

This work explains one way in which HRSI stereopairs can address the need for forest structure characterization across broad extents with fine spatial detail. These contributions can become part of a broader strategy that incorporates data from new spaceborne sensors for capturing the patterns of boreal and biome boundary forest structure at critical scales.

5. Conclusions

We applied automated stereogrammetry to stereopairs to produce HRSI DSM estimates of surface elevations in open canopy high-latitude biome boundary forest. Our results show that sun elevation angle at the time of stereopair acquisition influences the stereogrammetric surface elevation estimates, such that there are illumination conditions conducive for capturing elevations of surfaces either near the ground in open boreal canopies or associated with the vegetation canopy. For the open canopy forests across our study sites, the DSMs derived from stereopair acquisitions at sun elevation angles < 10° and also snow-free captured forest canopy surfaces, while those from acquisitions at sun elevations angles > 35° captured surfaces more closely associated with the ground (RMSEs < 0.68 m). At each site, these general types of DSMs were co-registered and differenced. Distributions of these height estimates at sample

forest locations coincide with reference plot-level mean tree heights (+/- 1 σ). Knowledge of HRSI acquisition solar geometry and snow cover can be used to understand and combine stereogrammetric surface elevation estimates to co-register and difference overlapping DSMs, providing a means to map forest height at fine scales, resolving the vertical structure of groups of trees from spaceborne platforms in open canopy boreal forests.

6. Acknowledgements

We acknowledge Oleg Alexandrov for the background information he provided on the Ames Stereo Pipeline software, Dan Duffy, Scott Sinno and Garrison Vaughan for their assistance working in the NASA Center for Climate Simulation's ADAPT high performance computing environment, and Viacheslav Kharuk, Sergey Im, Pasha Oskorbin and Mukhtar Naurzbaev for their collaboration with the field expeditions to the Larch forests in northern Siberia. This work was funded by the NASA Terrestrial Ecology Program, grant number NNH13ZDA001N-CARBON.

References

Aguilar, M. A., del Mar Saldana, M., & Aguilar, F. J. (2014). Generation and quality assessment of stereo-extracted DSM from GeoEye-1 and WorldView-2 imagery. *IEEE Transactions on Geoscience and Remote Sensing*, *52*(2), 1259–1271.

Aguilar, M. A., Saldaña, M. M., & Aguilar, F. J. (2013). GeoEye-1 and WorldView-2 pan-sharpened imagery for object-based classification in urban environments. *International Journal of Remote Sensing*. http://doi.org/10.1080/01431161.2012.747018

Arnot, C., & Fisher, P. (2007). Mapping the ecotone with fuzzy sets. *Geographic Uncertainty in Environmental Security*, 19–32.

Asner, G. (2003). Canopy shadow in IKONOS satellite observations of tropical forests and savannas. *Remote Sensing of Environment*, *87*(4), 521–533. http://doi.org/10.1016/j.rse.2003.08.006

Baltsavias, E., Gruen, A., Eisenbeiss, H., Zhang, L., & Waser, L. T. (2008). High- quality image

matching and automated generation of 3D tree models. *International Journal of Remote Sensing*, *29*(5), 1243–1259. http://doi.org/10.1080/01431160701736513

Benaglia, T., Chauveau, D., & Hunter, D. (2009). mixtools: An R package for analyzing finite mixture models. *Journal of Statistical Software*, *32*(6), 1–29.

Berner, L. T., Beck, P. S. A., Loranty, M. M., Alexander, H. D., Mack, M. C., & Goetz, S. J. (2012). Cajander larch (*Larix cajanderi*) biomass distribution, fire regime and post-fire recovery in northeastern Siberia. *Biogeosciences*, *9*(10), 3943–3959. http://doi.org/10.5194/bg-9-3943-2012

Bonan, G. B., Chapin, F. S., & Thompson, S. L. (1995). Boreal forest and tundra ecosystems as components of the climate system. *Climatic Change*, *29*(2), 145–167.

Bonan, G. B., Pollard, D., & Thompson, S. L. (1992). Effects of boreal forest vegetation on global climate. *Nature*, *359*.

Bunn, A. G., Hughes, M. K., & Salzer, M. W. (2011). Topographically modified tree-ring chronologies as a potential means to improve paleoclimate inference. *Climatic Change*, *105*(3-4), 627–634. http://doi.org/10.1007/s10584-010-0005-5

Case, B. S., & Duncan, R. P. (2014). A novel framework for disentangling the scale-dependent influences of abiotic factors on alpine treeline position. *Ecography*, *37*(9), 838–851. http://doi.org/10.1111/ecog.00280

Chen, H., Cloude, S.R., & Goodenough, D.G. (2016). Forest canopy height estimation using Tandem-X coherence data. *IEEE Journal of Selected Topics in Applied Earth Observations and Remote Sensing*, 9(7), 3177 - 3188.

Chopping, M. (2011). CANAPI: canopy analysis with panchromatic imagery. *Remote Sensing Letters*, *2*(1), 21–29. http://doi.org/10.1080/01431161.2010.486805

Coburn, C. A., & Roberts, A. C. B. (2004). A multiscale texture analysis procedure for improved forest stand classification. *International Journal of Remote Sensing*, *25*(20), 4287–4308. http://doi.org/10.1080/0143116042000192367

Dalen, L., & Hofgaard, A. (2005). Differential regional treeline dynamics in the Scandes Mountains.

Arctic, Antarctic, and Alpine Research, *37*(3), 284–296.

Danby, R. K., & Hik, D. S. (2007). Variability, contingency and rapid change in recent subarctic alpine tree line dynamics. *Journal of Ecology*, *95*(2), 352–363. http://doi.org/10.1111/j.1365-2745.2006.01200.x

DigitalGlobe. (2014). Geolocation Accuracy of WorldView Products. *White Paper*, 1–10.

Dolloff, J., & Settergren, R. (2010). An assessment of WorldView-1 positional accuracy based on fifty contiguous stereo pairs of imagery. *Photogrammetric Engineering & Remote Sensing*, *76*(8), 935–943.

Dubayah, R., Goetz, S. J., & Blair, J. B. (2014, December). The Global Ecosystem Dynamics Investigation. *AGU Fall Meeting Abstracts*. San Francisco, CA.

Duncanson, L. I., Dubayah, R. O., Cook, B. D., Rosette, J., & Parker, G. (2015). The importance of spatial detail: Assessing the utility of individual crown information and scaling approaches for lidar-based biomass density estimation. *Remote Sensing of Environment*, *168*(C), 102–112. http://doi.org/10.1016/j.rse.2015.06.021

Duong, H., Lindenbergh, R., Pfeifer, N., Vosselman, G. (2009). ICESat full-waveform altimetry compared to airborne laser scanning altimetry over The Netherlands. *IEEE Transactions on Geoscience and Remote Sensing*, 47(10), 3365 - 3378.

Epiphanio, J., & Huete, A. R. (1995). Dependence of NDVI and SAVI on sun/sensor geometry and its effect on fAPAR relationships in alfalfa. *Remote Sensing of Environment*, *51*, 351–360.

Epstein, H. E., Beringer, J., Gould, W. A., Lloyd, A. H., Thompson, C. D., Chapin, F. S., et al. (2004). The nature of spatial transitions in the Arctic. *Journal of Biogeography*, *31*(12), 1917–1933.

Frost, G. V., Epstein, H. E., & Walker, D. A. (2014). Regional and landscape-scale variability of Landsat-observed vegetation dynamics in northwest Siberian tundra. *Environmental Research Letters*, *9*(2), 025004. http://doi.org/10.1088/1748-9326/9/2/025004

Harper, K. A., Danby, R. K., De Fields, D. L., Lewis, K. P., Trant, A. J., Starzomski, B. M., et al. (2011). Tree spatial pattern within the forest–tundra ecotone: a comparison of sites across Canada. *Canadian*

718 *Journal of Forest Research*, *41*(3), 479–489. http://doi.org/10.1139/X10-221
719 Harsch, M. A., & Bader, M. Y. (2011). Treeline form - a potential key to understanding treeline
720 dynamics. *Global Ecology and Biogeography*, *20*(4), 582–596. http://doi.org/10.1111/j.1466-
721 8238.2010.00622.x
722 Harsch, M., Hulme, P., McGlone, M., & Duncan, R. (2009). Are treelines advancing? A global meta-
723 analysis of treeline response to climate warming. *Ecology Letters*, *12*(10), 1040–1049.
724 Hobi, M. L., & Ginzler, C. (2012). Accuracy Assessment of Digital Surface Models Based on
725 WorldView-2 and ADS80 Stereo Remote Sensing Data. *Sensors*, *12*(12), 6347–6368.
726 http://doi.org/10.3390/s120506347
727 Hofgaard, A., & Wilmann, B. (2002). Plant distribution pattern across the forest-tundra ecotone: the
728 importance of treeline position. *Ecoscience*, *9*(2), 375–385.
729 Hofgaard, A., Harper, K. A., & Golubeva, E. (2012). The role of the circumarctic forest–tundra ecotone
730 for Arctic biodiversity. *Biodiversity*, *13*(3-4), 174–181.
731 http://doi.org/10.1080/14888386.2012.700560
732 Holtmeier, F. K. (2009). Mountain Timberlines: Ecology, Patchiness and Dynamics. Netherlands: Kluwer
733 Academic Publishers.
734 Holtmeier, F.-K., & Broll, G. (2005). Sensitivity and response of northern hemisphere altitudinal and
735 polar treelines to environmental change at landscape and local scales. *Global Ecology and*
736 *Biogeography*, *14*(5), 395–410.
737 Honkavaara, E., Arbiol, R., Markelin, L., Martinez, L., Cramer, M., Bovet, S., et al. (2009). Digital
738 Airborne Photogrammetry—A New Tool for Quantitative Remote Sensing?—A State-of-the-Art
739 Review On Radiometric Aspects of Digital Photogrammetric Images. *Remote Sensing*, *1*(4), 577–
740 605. http://doi.org/10.3390/rs1030577
741 Hufkens, K., Scheunders, P., & Ceulemans, R. (2009). Ecotones in vegetation ecology: methodologies
742 and definitions revisited. *Ecological Research*, *24*(5), 977–986. http://doi.org/10.1007/s11284-009-
743 0584-7

744 Jeong, J., and T. Kim, 2014. Analysis of dual-sensor stereo geometry and its positioning accuracy.
745 *Photogrammetric Engineering & Remote Sensing*, 80(7):653-662.
746 Jeong, J., and T. Kim, 2016. Quantitative estimation and validation of the effects of the convergence,
747 bisector elevation, and asymmetry angles on the positioning accuracies of satellite stereo pairs.
748 *Photogrammetric Engineering & Remote Sensing*, 82(8):625-633.
749 Kane, V., Gillespie, A., McGaughey, R., Lutz, J., Ceder, K., Franklin, J., 2008. Interpretation and
750 topographic compensation of conifer canopy self-shadowing. *Remote Sens. Environ.* 112 (10):3820–
751 3832. http://dx.doi.org/10.1016/j.rse.2008.06.001.
752 Kayitakire, F., Hamel, C., & Defourny, P. (2006). Retrieving forest structure variables based on image
753 texture analysis and IKONOS-2 imagery. *Remote Sensing of Environment*, *102*(3-4), 390–401.
754 http://doi.org/10.1016/j.rse.2006.02.022
755 Kimes, D. S. (1983). Dynamics of directional reflectance factor distributions for vegetation canopies.
756 *Applied Optics*, *22*(9), 1364–1372.
757 Kirdyanov, A. V., Prokushkin, A. S., & Tabakova, M. A. (2013). Tree-ring growth of Gmelin larch under
758 contrasting local conditions in the north of Central Siberia. *Dendrochronologia*.
759 http://doi.org/10.1016/j.dendro.2012.10.003
760 Korpela, I., Heikkinen, V., Honkavaara, E., Rohrbach, F., & Tokola, T. (2011). Variation and directional
761 anisotropy of reflectance at the crown scale — Implications for tree species classification in digital
762 aerial images. *Remote Sensing of Environment*, *115*(8), 2062–2074.
763 http://doi.org/10.1016/j.rse.2011.04.008
764 Lagomasino, D., Fatoyinbo, T., Lee, S.-K., & Simard, M. (2015). High-resolution forest canopy height
765 estimation in an African blue carbon ecosystem. *Remote Sensing in Ecology and Conservation*, *1*(1),
766 51–60. http://doi.org/10.1002/rse2.3
767 Lamonaca, A., Corona, P., & Barbati, A. (2008). Exploring forest structural complexity by multi-scale
768 segmentation of VHR imagery. *Remote Sensing of Environment*, *112*(6), 2839–2849.
769 http://doi.org/10.1016/j.rse.2008.01.017

Lloyd, A. H., Bunn, A. G., & Berner, L. T. (2011). A latitudinal gradient in tree growth response to climate warming in the Siberian taiga. *Global Change Biology*, *17*(5), 1935–1945. http://doi.org/10.1111/j.1365-2486.2010.02360.x

Mallinis, G., Koutsias, N., Tsakiri-Strati, M., & Karteris, M. (2008). Object-based classification using Quickbird imagery for delineating forest vegetation polygons in a Mediterranean test site. *ISPRS Journal of Photogrammetry and Remote Sensing*, *63*(2), 237–250. http://doi.org/10.1016/j.isprsjprs.2007.08.007

Manninen, T., Korhonen, L., Voipio, P., Lahtinen, P., & Stenberg, P. (2009). Leaf Area Index (LAI) Estimation of Boreal Forest Using Wide Optics Airborne Winter Photos. *Remote Sensing*, *1*(4), 1380–1394. http://doi.org/10.3390/rs1041380

Montesano, P. M., Rosette, J., Sun, G., North, P., Nelson, R. F., Dubayah, R. O., et al. (2015). The uncertainty of biomass estimates from modeled ICESat-2 returns across a boreal forest gradient. *Remote Sensing of Environment*, *158*, 95–109. http://doi.org/10.1016/j.rse.2014.10.029

Montesano, P. M., Sun, G., Dubayah, R. O., & Ranson, K. J. (2016). Spaceborne potential for examining taiga–tundra ecotone form and vulnerability. *Biogeosciences*, *13*(13), 3847–3861. http://doi.org/10.5194/bg-13-3847-2016

Montesano, P., Sun, G., Dubayah, R., & Ranson, K. (2014). The Uncertainty of Plot-Scale Forest Height Estimates from Complementary Spaceborne Observations in the Taiga-Tundra Ecotone. *Remote Sensing*, *6*(10), 10070–10088. http://doi.org/10.3390/rs61010070

Moratto, Z. M., Broxton, M. J., Beyer, R. A., Lundy, M., & Husmann, K. (2010). Ames Stereo Pipeline, NASA's open source automated stereogrammetry software. *41st Lunar and Planetary Science Conference Abstracts*.

Neigh, C. S. R., Masek, J. G., Bourget, P., Rishmawi, K., Zhao, F., Huang, C., et al. (2016). Regional rates of young US forest growth estimated from annual Landsat disturbance history and IKONOS stereo imagery. *Remote Sens. Environ*. 173 (C):282–293. http://dx.doi. org/10.1016/j.rse.2015.09.007

Neigh, C. S., Masek, J. G., & Nickeson, J. E. (2013a). High- Resolution Satellite Data Open for

Government Research. *Eos, Transactions American Geophysical Union*, *94*(13), 121–123.

Neigh, C. S., Nelson, R. F., Ranson, K. J., Margolis, H. A., Montesano, P. M., Sun, G., et al. (2013b). Taking stock of circumboreal forest carbon with ground measurements, airborne and spaceborne lidar. *Remote Sensing of Environment*, *137*, 274–287. http://doi.org/10.1016/j.rse.2013.06.019

Neigh, C., Masek, J., Bourget, P., Cook, B., Huang, C., Rishmawi, K., & Zhao, F. (2014). Deciphering the Precision of Stereo IKONOS Canopy Height Models for US Forests with G-LiHT Airborne lidar. *Remote Sensing*, *6*(3), 1762–1782. http://doi.org/10.3390/rs6031762

Nelson, R., Ranson, K. J., Sun, G., Kimes, D. S., Kharuk, V., & Montesano, P. (2009). Estimating Siberian timber volume using MODIS and ICESat/GLAS. *Remote Sensing of Environment*, *113*(3), 691–701. http://doi.org/10.1016/j.rse.2008.11.010

Neuenschwander, A., & Magruder, L. (2016). The Potential Impact of Vertical Sampling Uncertainty on ICESat-2/ATLAS Terrain and Canopy Height Retrievals for Multiple Ecosystems. *Remote Sensing*, *8*(12), 1039. http://doi.org/10.3390/rs8121039

Olesk, A., Praks, J., Antropov, O., Zalite, K., Arumae, T., & Voormansik, K. (2016). Interferometric SAR coherence models for characterisation of hemiboreal forests using Tandem-X data. *Remote Sensing*, 8, 700 - 723

Osawa, A., & Kajimoto, T. (2009). Development of Stand Structure in Larch Forests. In *Permafrost Forests* (Vol. 209, pp. 123–148). Dordrecht: Ecological Studies. http://doi.org/10.1007/978-1-4020-9693-8_7

Ozdemir, I., & Karnieli, A. (2011). Predicting forest structural parameters using the image texture derived from WorldView-2 multispectral imagery in a dryland forest, Israel. *International Journal of Applied Earth Observations and Geoinformation*, *13*(5), 701–710. http://doi.org/10.1016/j.jag.2011.05.006

Persson, H., Wallerman, J., & Olsson, H. (2013). Estimating forest biomass and height using optical stereo satellite data and a DTM from laser scanning data. *Canadian Journal of Remote Sensing*, 39(3), 251 - 262.

Poon, J., Fraser, C., & Zhang, C. (2007). Digital surface models from high resolution satellite imagery.

Photogrammetric Engineering and Remote Sensing, 73(11), 1225 - 1231.

Qi, W., & Dubayah, R. O. (2016). Combining Tandem-X InSAR and simulated GEDI lidar observations for forest structure mapping. *Remote Sensing of Environment*, *187*, 253–266. http://doi.org/10.1016/j.rse.2016.10.018

R Core Team (2013). R: A language and environment for statistical computing. R Foundation for Statistical Computing, Vienna, Austria. ISBN 3-900051-07-0, URL http://www.R-project.org/.

Ranson, K. J., Daughtry, C., & Biehl, L. L. (1985). Sun-view angle effects on reflectance factors of corn canopies. *Remote Sensing of Environment*, *18*, 147–161.

Shean, D. E., Alexandrov, O., Moratto, Z. M., Smith, B. E., Joughin, I. R., Porter, C., & Morin, P. (2016). ISPRS Journal of Photogrammetry and Remote Sensing. *ISPRS Journal of Photogrammetry and Remote Sensing*, *116*(C), 101–117. http://doi.org/10.1016/j.isprsjprs.2016.03.012

Soja, A., Tchebakova, N., French, N., Flannigan, M., Shugart, H., Stocks, B., et al. (2007). Climate-induced boreal forest change: predictions versus current observations. *Global and Planetary Change*, *56*(3-4), 274–296.

Sun, G., Ranson, K.K., Kimes, D.S., Blair, J.B., & Kovacs, K. (2008). Forest vertical structure from GLAS: an evaluation using LVIS and SRTM data. *Remote Sensing of Environment*, 112(1), 107-117.

Stysley, P. R., Coyle, D. B., Kay, R. B., Frederickson, R., Poulios, D., Cory, K., & Clarke, G. (2015). Long term performance of the High Output Maximum Efficiency Resonator (HOMER) laser for NASA's Global Ecosystem Dynamics Investigation (GEDI) lidar. *Optics and Laser Technology*, *68*(C), 67–72. http://doi.org/10.1016/j.optlastec.2014.11.001

Vega, C., & St-Onge, B. (2008). Height growth reconstruction of a boreal forest canopy over a period of 58 years using a combination of photogrammetric and lidar models. *Remote Sensing of Environment*, *112*(4), 1784–1794. http://doi.org/10.1016/j.rse.2007.09.002

Wang, L., Sousa, W. P., Gong, P., & Biging, G. S. (2004). Comparison of IKONOS and QuickBird images for mapping mangrove species on the Caribbean coast of Panama. *Remote Sensing of Environment*, *91*(3-4), 432–440. http://doi.org/10.1016/j.rse.2004.04.005

Widlowski, J. L., Pinty, B., & Gobron, N. (2001). Detection and characterization of boreal coniferous forests from remote sensing data. *Journal of Geophysical Research*, *106*(D24), 33–405–33–419.

Wolter, P. T., Townsend, P. A., & Sturtevant, B. R. (2009). Estimation of forest structural parameters using 5 and 10 meter SPOT-5 satellite data. *Remote Sensing of Environment*, *113*, 2019–2036. http://doi.org/10.1016/j.rse.2009.05.009

Wulder, M. A., Hall, R. J., & Coops, N. C. (2004). High spatial resolution remotely sensed data for ecosystem characterization. *Bioscience*, *54*(6), 511–521.

Wulder, M. A., Ortlepp, S. M., & White, J. C. (2008). Impact of sun-surface-sensor geometry upon multitemporal high spatial resolution satellite imagery. *Canadian Journal of Remote Sensing*, *34*(5), 455–461.

Wulder, M. A., White, J. C., Nelson, R. F., Næsset, E., Ørka, H. O., Coops, N. C., et al. (2012). lidar sampling for large-area forest characterization: A review. *Remote Sensing of Environment*, *121*, 196–209. http://doi.org/10.1016/j.rse.2012.02.001

Zwally, H. J., Schutz, B., Abdalati, W., Abshire, J., Bentley, C., Brenner, A., et al. (2002). ICESat's laser measurements of polar ice, atmosphere, ocean, and land. *Journal of Geodynamics*, *34*(3), 405–445.

Zwally, J, H., Schutz, R., Bentley, C., Bufton, J., Herring, T., et al. (2014). GLAS/ICESat L2 Global Land Surface Altimetry Data, Version 34. NASA National Snow and Ice Data Center Distributed Active Archive Center. http://doi.org/10.5067/ICESAT/GLAS/DATA227

Ørka, H. O., Wulder, M. A., Gobakken, T., & Næsset, E. (2012). Subalpine zone delineation using lidar and Landsat imagery. *Remote Sensing of Environment*, *119*(C), 11–20. http://doi.org/10.1016/j.rse.2011.11.023